Supporting Information

Self-Powered Hazard Warning Alarm System based on CNT/Cellulose Aerogel TENG for Firefighter Protection.

Table S1. Comparison of state-of-the-art aerogel-based triboelectric nanogenerators (TENGs) and protective materials.

Reference	Material system	V_{OC}(V)	I_{SC}(μA)	Thermal Conductivity, λ (W/(m·K))	Notes	Ref.
Li et al., 2024, AFM	silica/ANF aerogel fibers	15.8	0.18	0.033	PCWA-TENG	[49]
Sun et al., 2024, AFM	MXene-Based Composite aerogels	10	1.6	0.022	MPS-UHP -TENG	[46]
Wang et al., 2024, Small	CNFs/PMSQ aerogels	80	1.2	17	LTC-S3-TENG	[50]
Hu et al., 2025, CEJ	ZIF-67/Zylon aerogel fabric	70.8	2.0	0.042	ZIF-67/Zylon-TENG	[47]
Jalali et al., 2025, Carbohydrate Polymers	3D-printed chitosan/MXene aerogels	110	1.9	0.025	3D-printed TENG	[48]
This work	CCHA aerogels	210	30	0.0077	CCHA-TENG	

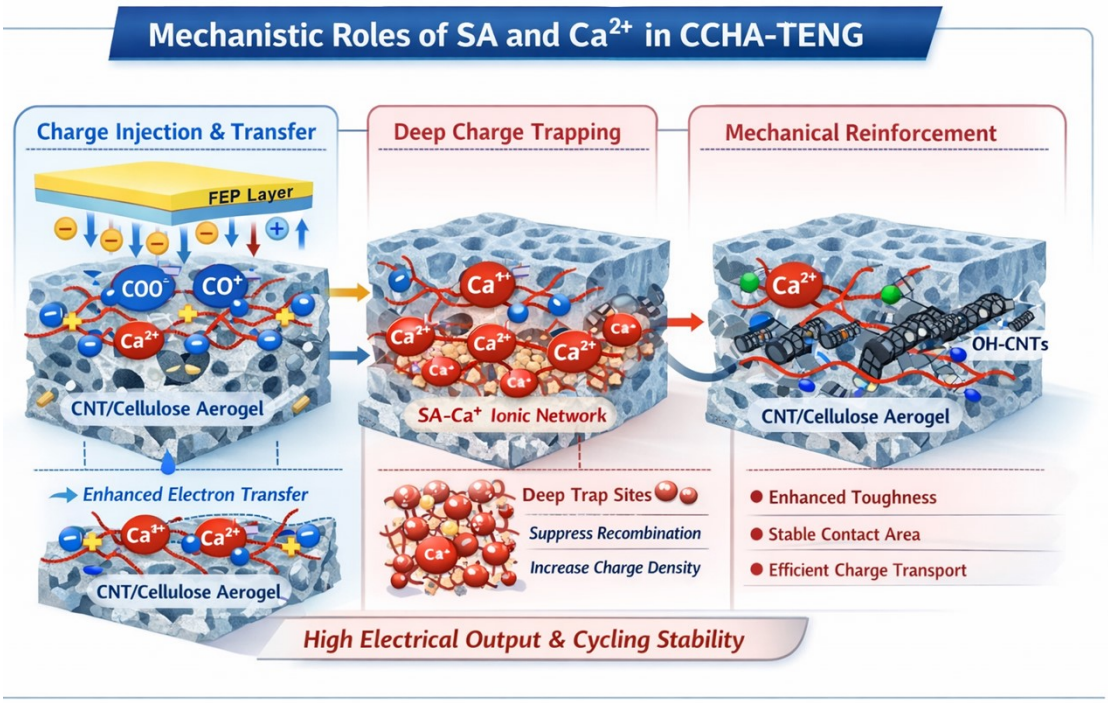

Fig. S2 Schematic illustration of the multifunctional roles of the SA–Ca^{2+} ionic crosslinking network in the CCHA-TENG.

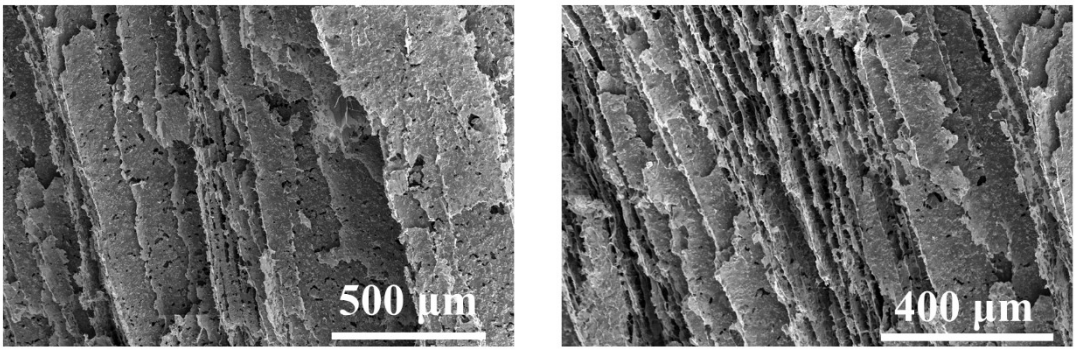

Fig. S3 Cross-sectional SEM images of the S1 CCHA aerogel

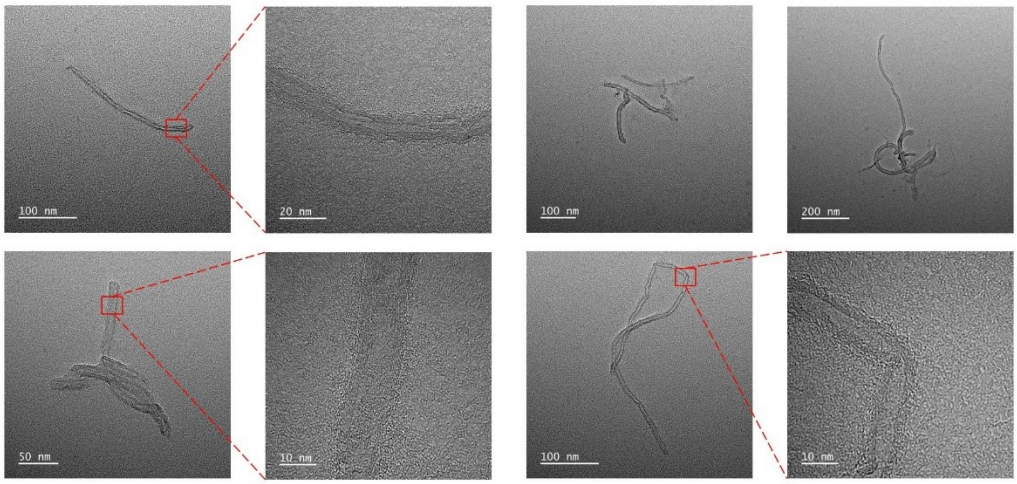

Fig. S4 TEM images showing the dispersion of CNTs within the CCHA composite aerogel matrix.

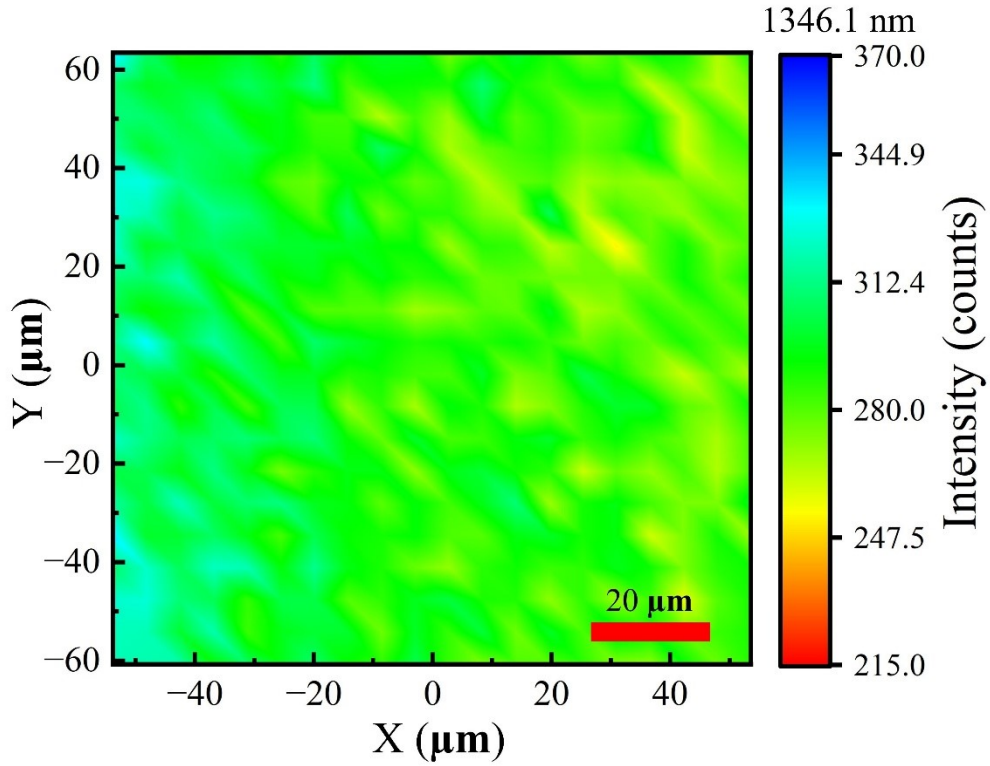

Fig. S5 Raman mapping of the D band (~1346 cm^{-1}) collected over a 60 × 60 $μm^2$ region of the CCHA composite aerogel.

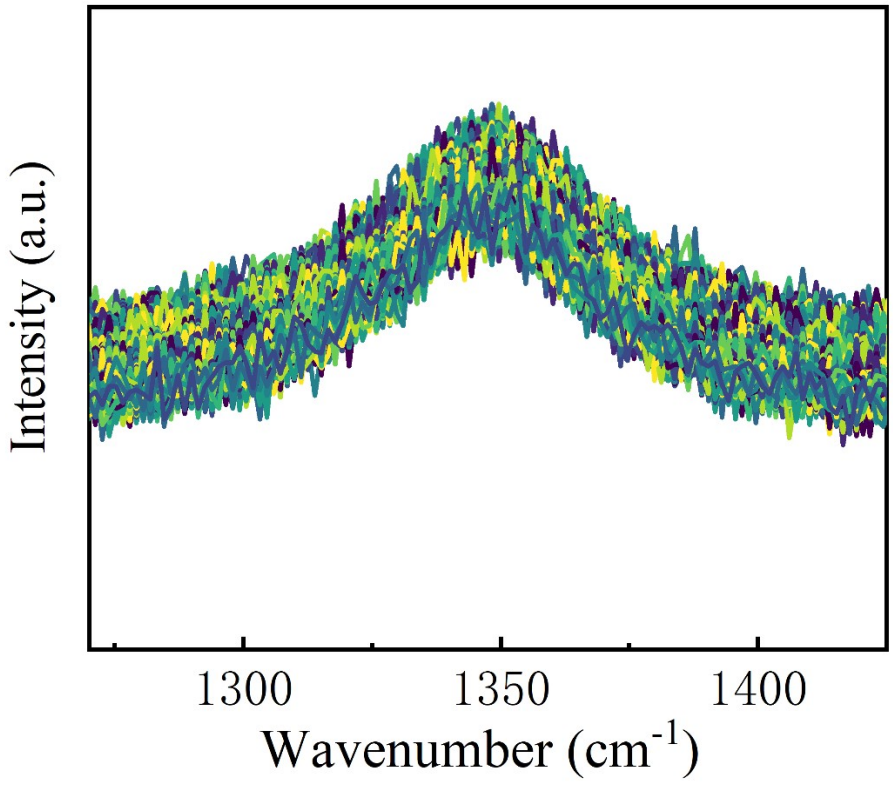

Fig. S6 Raman spectra obtained from different mapping points within the Raman mapping area of the CCHA composite aerogel.

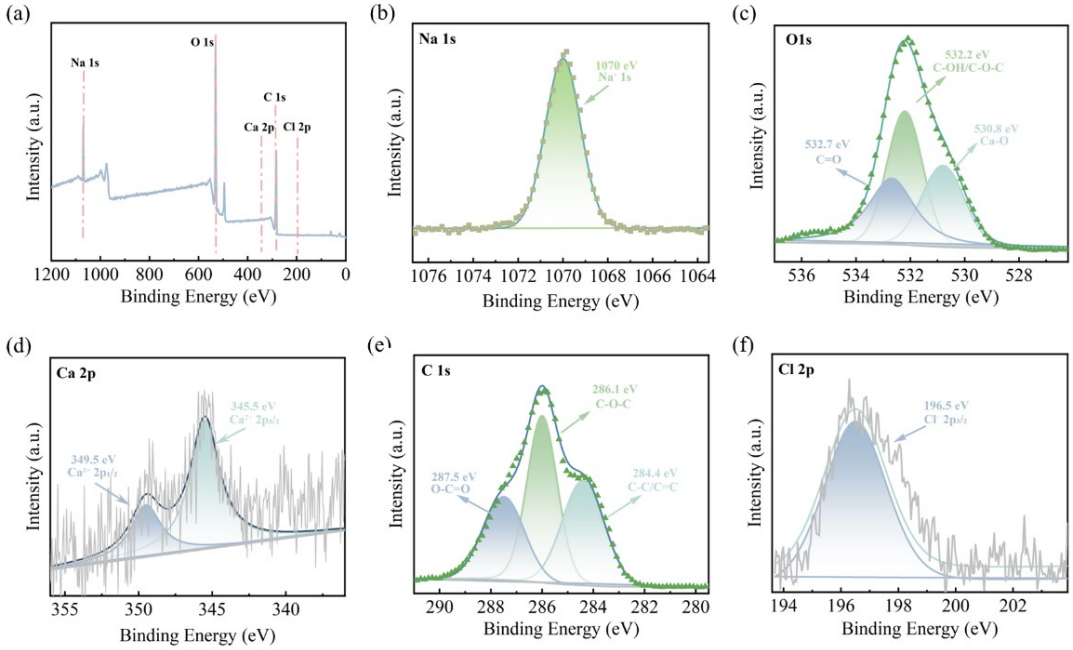

Fig. S7 X-ray photoelectron spectroscopy (XPS) analysis of the composite aerogel: (a) survey spectrum, (b) Na 1s, (c) O 1s, (d) Ca 2p, (e) C 1s, and (f) Cl 2p.

Table S8. The pore parameters of CCHA were measured by mercury intrusion.

Samples	Porosity volume	Average aperture 4 V/A (nm)	Median aperture V (nm)	Median aperture A (nm)	Total pore volume (mL/g)	Total pore area (m^2/g)
CCHA	93.41	1337.93	17462.76	37.19	10.95	32.73

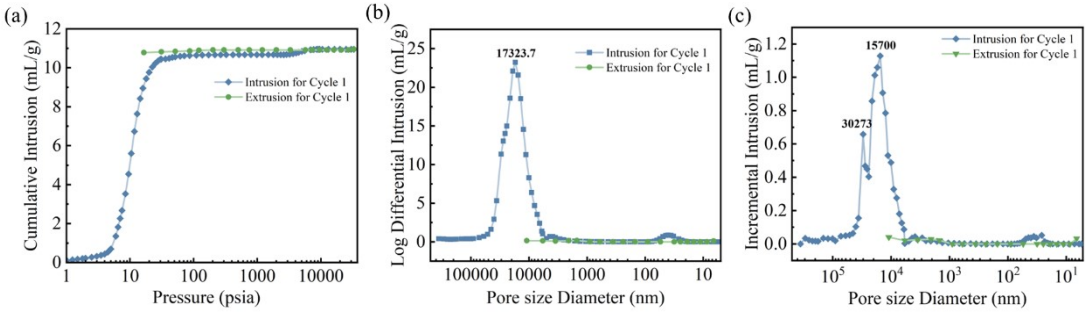

Fig. S9 Mercury intrusion porosimetry (MIP) analysis of the CCHA aerogel: (a) Cumulative intrusion volume as a function of pressure. (b) Log-differential intrusion curve as a function of pore size diameter. (c) Differential pore size distribution of the CCHA aerogel.

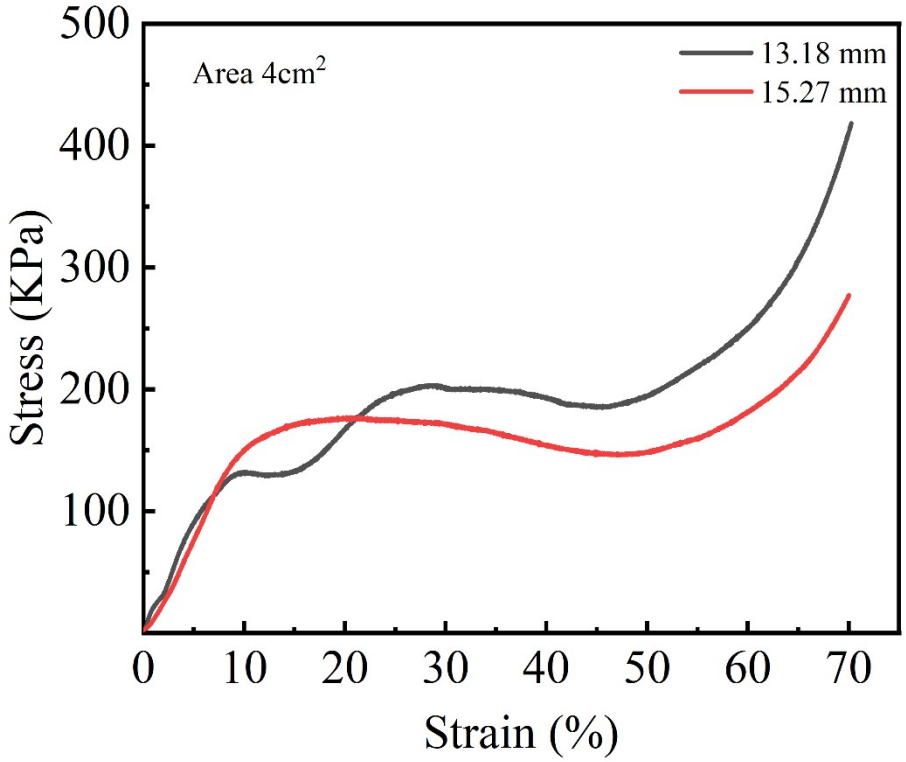

Fig. S10 Uniaxial compressive stress–strain curves of CCHA aerogels with identical cross-sectional areas (4 cm^2) but different initial heights (13.18 mm and 15.27 mm).

Fig. S11 Schematic Diagram of the Working Principle of Thermal Imaging.

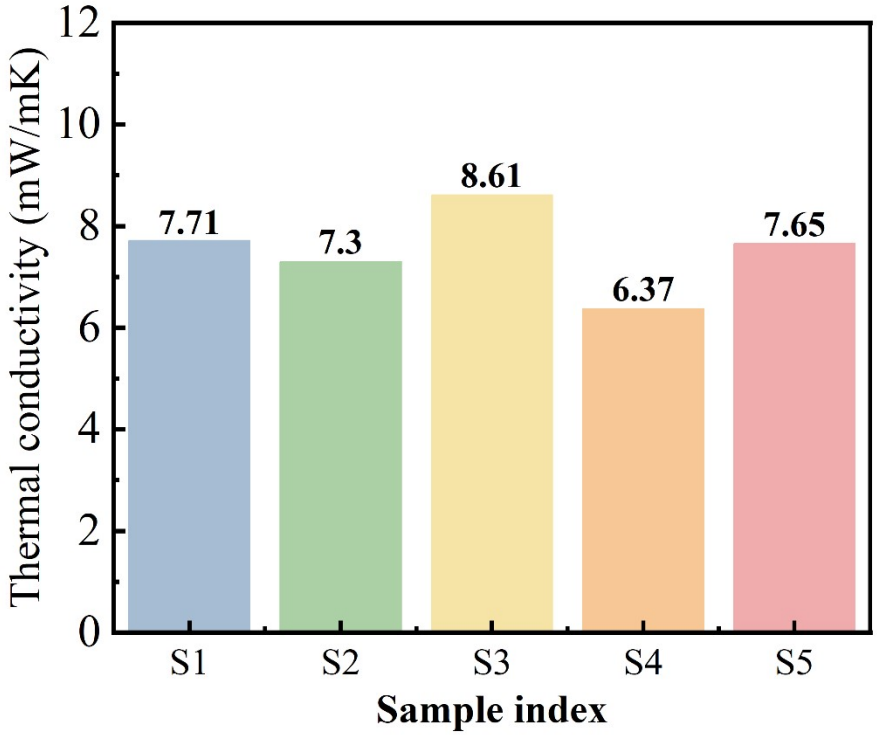

Fig. S12 Reproducibility test of radial thermal conductivity of CCHA aerogels.

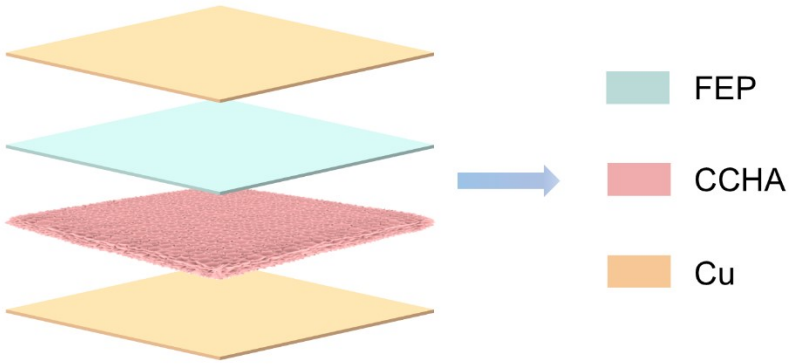

Fig. S13 Structure of CCHA-TENG.

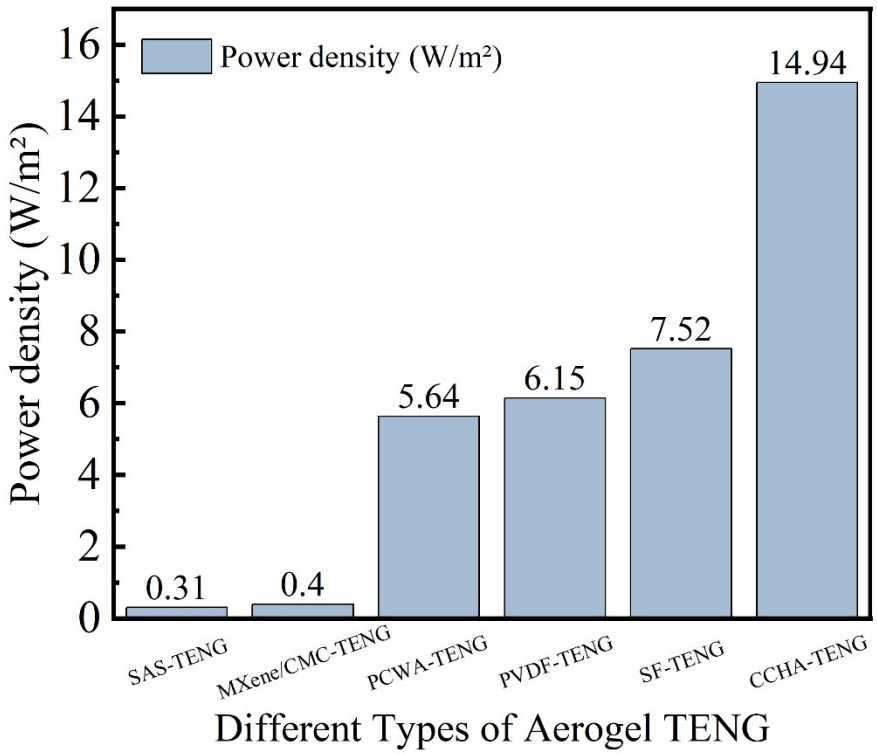

Fig. S14 Comparison of the reported power densities of representative aerogel-based TENGs. The maximum power density in each case was calculated at the optimal load resistance. Differences in testing conditions may exist; therefore, this comparison serves as qualitative benchmarking rather than a strict quantitative evaluation.

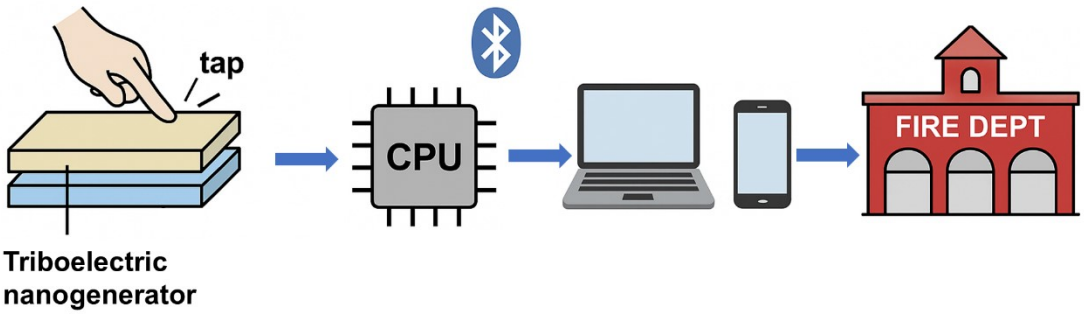

Fig. S15 Operating modes of CCHA-TENG wireless transmission.

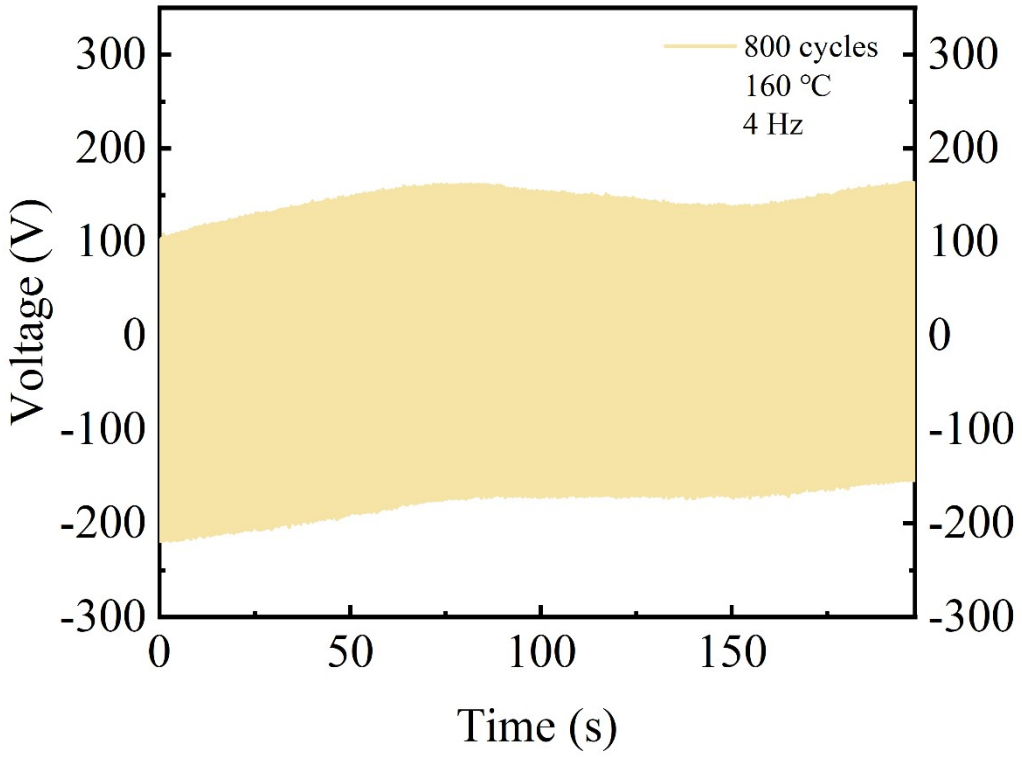

Fig. S16 Cyclic durability of the CCHA-TENG after thermal treatment at 160 °C.